Challenges and Approaches to Quantitative Therapy Response Assessment in Glioblastoma Multiforme Using the Novel Apoptosis Positron Emission Tomography Tracer F-18 ML-10[1]

Matthew J. Oborski*, Charles M. Laymon*,†, Yongxian Qian†, Frank S. Lieberman‡, Arden D. Nelson§ and James M. Mountz†

*Department of Bioengineering, University of Pittsburgh, Pittsburgh, PA; †Department of Radiology, University of Pittsburgh, Pittsburgh, PA; ‡Department of Neurology and Department of Medicine, Division of Hematology/Oncology, University of Pittsburgh School of Medicine, Pittsburgh, PA; §MIM Software Inc, Cleveland, OH

Abstract

Evaluation of cancer-therapy efficacy at early time points is necessary for realizing the goal of delivering maximally effective treatment. Molecular imaging with carefully selected tracers and methodologies can provide the means for realizing this ability. Many therapies are aimed at inducing apoptosis in malignant tissue; thus, the ability to quantify apoptosis *in vivo* may be a fruitful approach. Apoptosis rate changes occur on a fast time scale, potentially allowing correspondingly rapid decisions regarding therapy value. However, quantification of tissue status based on apoptosis imaging is complicated by this time scale and by the spatial heterogeneity of the process. Using the positron emission tomography (PET) tracer 2-(5-fluoro-pentyl)-2-methyl-malonic acid (F-18 ML-10), we present methods of voxelwise analysis yielding quantitative measures of apoptosis changes, parametric apoptosis change images, and graphical representation of apoptotic features. A method of deformable registration to account for anatomic changes between scan time points is also demonstrated. Overall apoptotic rates deduced from imaging depend on tumor density and the specific rate of apoptosis, a situation resulting in an ambiguity in the source of observed image-based changes. The ambiguity may be resolved through multimodality imaging. An example of intracellular sodium magnetic resonance imaging coupled with F-18 ML-10 PET is provided.

Translational Oncology (2014) 7, 111–119

Introduction

Every year, 22,500 new cases of primary brain tumor are diagnosed in adults in the United States of which 70% are malignant glioblastoma multiforme (GBM) [1,2]. With treatment, median survival is only 12 to 15 months for GBM and 2 to 5 years for anaplastic astrocytoma. Motivated by these poor outcomes, new brain cancer therapies are actively being developed and evaluated. There is a concurrent and pressing need for methods for accurate and timely assessment of treatment response to both facilitate therapy development and, ultimately, improve clinical management. However, the development of crucially needed novel therapies for malignant gliomas as well as improved clinical management critically depends on the availability of quantitative imaging biomarkers that are predictive of early therapy response.

Because the main purpose of effective cancer therapy is to eliminate cancer cells, imaging of apoptosis offers a direct way to image therapy response [3]. This programmed form of cell death is regulated by several pathways and leads to a removal of the dead cell by macrophages. Currently, only two apoptosis radiopharmaceuticals have been studied in clinical trials for follow-up of tumor treatment: Tc-99m or I-123–labeled annexin V and F-18–labeled 2-(5-fluoro-pentyl)-2-methyl-malonic acid (F-18 ML-10).

F-18 ML-10 is a low–molecular mass compound [molecular weight (MW) = 206 Da] with an alkyl-malonic acid motif as recognition site and a small aliphatic "tail" to which F-18 is bound [5]. Although the radiosynthesis comprises two steps, both can be performed rapidly and have a high yield, resulting in a tracer that is suitable for routine clinical practice. *In vitro*, tritiated ML-10 (H-3 ML-10) has been shown to selectively cross the plasma membrane of cells undergoing apoptosis (localizing predominantly in the cytoplasm) while being excluded from viable cells [6]. These studies suggest that cell plasma membrane depolarization drives the observed selectivity of H-3 ML-10 for apoptotic cells [6]. Importantly, fluorescence microscopy imaging has shown the selective detection of apoptosis to be true across multiple cell lines and multiple apoptosis-inducing therapies [6]. Furthermore, preclinical F-18 ML-10 phosphorimaging studies of mouse stroke tissue sections demonstrated a spatial correlation between F-18 ML-10 uptake in the infarct region of the mouse brain and terminal deoxynucleotidyl transferase 2′-deoxyuridine 5′-triphosphate (dUTP) nick end labeling (which detects characteristic apoptotic DNA fragmentation) histologic analysis of corresponding tissue sections [5].

In humans, F-18 ML-10 biodistribution shows no specific uptake in nontarget organs or tissues and a desirable rapid clearance from blood through the kidneys [4]. It also exhibits high stability *in vivo* [7]. Specifically, an analysis of plasma samples from eight human subjects found a 97.5% ± 0.4% unchanged F-18 ML-10 fraction 150 minutes post-injection [7]. Moreover, Oborski et al. [8] observed a changing pattern of F-18 ML-10 tracer distribution on PET in a human patient with GBM at baseline (BL) and at a therapy [radiotherapy (RT) plus temozolomide chemotherapy] response assessment time point, with comparatively low background F-18 ML-10 uptake in normal brain. Similarly, in studies evaluating F-18 ML-10 PET as a novel tool for the early detection of response of brain metastases to whole-body radiation therapy at 30 Gy, patients underwent two F-18 ML-10 PET scans, the first before therapy and the second after 9 or 10 fractions of RT (approximately 2 weeks from the start of therapy) [9]. Early treatment–induced changes in tumor F-18 ML-10 uptake were measured by voxel-based analysis and then evaluated by correlation analysis as predictors of the extent of later changes in tumor anatomic dimensions as seen on magnetic resonance imaging (MRI) scans 6 to 8 weeks after completion of therapy [9]. A highly significant correlation ($r = 0.9$) was found between early changes on the F-18 ML-10 scan and later changes in tumor anatomic dimensions [9].

Imaging therapy-induced apoptosis in tumors presents several challenges with regard to patient imaging protocols and quantitative response assessment methodology. For example, apoptosis is inherently a transient process; therefore, standardization of proper imaging protocols to assess for peak apoptotic response due to therapy is essential for being able to distinguish between therapy-induced apoptosis and native tumor cell turnover. This was first demonstrated by Blankenberg et al. [10] in a cyclophosphamide-treated murine lymphoma model. Treated tumors showed increased uptake compared to control 20 hours after therapy [10]. In terms of response assessment, accumulating evidence suggests that intratumoral heterogeneity is likely a key to understanding cancer treatment failure [11]. Tumors are composed of different subpopulations of cells that can harbor very different genotypes and phenotypes, such as differing degrees of differentiation, growth rates, and response to various therapeutic interventions [12]. Experimental evidence has also shown that vascular heterogeneity can be associated with disease progression, therapeutic response, and malignancy.

Due to the nature of the process, PET imaging of apoptosis requires specialized patient protocols and analysis methodologies. In this article, we demonstrate a set of approaches to quantifying therapeutic response assessment in the context of GBM subjects receiving F-18 ML-10 PET scans.

Materials and Methods

Subjects

This research was performed under the United States Food and Drug Administration (US FDA) Investigational New Drug program with University of Pittsburgh Institutional Review Board approval. After providing written informed consent, six subjects with newly diagnosed or first late recurrence of GBM were recruited for this study. For each patient, treatment consists of RT (200 cGy fractions per day to a total dose of 60 Gy) and temozolomide (75 mg/m^2) on days 1 to 42 and adjuvant chemotherapy with temozolomide (75 mg/m^2) on days 1 to 21 of 12 28-day cycles, beginning on about day 72.

Imaging Protocol

The imaging protocol called for subjects to undergo PET and MRI scanning sessions at BL, approximately 1 to 2 weeks before therapy initiation. An identical early therapy assessment (ETA) scan session was also performed approximately 14 ± 3 days after therapy initiation. We present results from four subjects at BL and the ETA scan session. Table 1 contains subject characteristics for all four subjects, including subject age at time of diagnosis, and overall survival (in months) from the time of each respective subject's therapy initiation.

PET acquisition protocol. The F-18 ML-10 tracer was produced at the University of Pittsburgh PET Facility Radiochemistry Laboratory (Pittsburgh, PA) using precursor supplied by Aposense Ltd (Petach-Tikva, Israel). PET scans were performed on a Siemens HR+ PET system (CTI/Siemens, Knoxville, TN) for a 30-minute interval commencing 120 minutes after injection of approximately 10 mCi of the F-18 ML-10 tracer. The 30-minute acquisition interval was subdivided into six 5-minute frames. Each data frame was reconstructed into a 128 × 128 × 63 (axial) matrix with voxel dimensions of 0.21 × 0.21 × 0.24 cm. Data were processed using the manufacturer's software using Fourier rebinning, followed by direct Fourier reconstruction. Images were smoothed with a 3-mm Hann filter. The process included corrections for attenuation, scatter, random coincidences, and dead time. The six resulting images (per scan) were examined for motion. A single 30-minute image was produced by averaging over frames.

MRI acquisition protocol. For each subject, at each time point, a series of MRI scans were acquired on a Siemens 3T Trio MR scanner. Data acquired included magnetization-prepared rapid acquisition

Table 1. Subjects.

Subject No.	Sex (Male/Female)	Age (Yr)	GBM Location	Overall Survival (Mo)
Subject 1	Male	64	Right frontal	17
Subject 2	Male	72	Left medial temporal	2
Subject 3	Female	58	Right parietal	13
Subject 4	Male	59	Left temporal	Alive at 11 mo

with gradient echo (MPRAGE) MRI and T_1-weighted contrast-enhanced MRI.

All sodium images were acquired on the 3 Tesla (3T) MRI scanners (MAGNETOM Trio Tim; Siemens Medical Solutions, Erlangen, Germany) with a dual-tuned (^{1}H-^{23}Na) volume head coil (Advanced Imaging Research, Cleveland, OH). Volume-fraction weighted concentration of bound sodium was quantified on a subtraction image related to sodium nuclei with biexponential T_2 relaxation. The subtraction image was produced by two single-quantum sodium images acquired at a very short echo time (TE) of TE_1 = 0.44 millisecond and a short echo time of TE_2 = 5 milliseconds, respectively. Each TE image was acquired in a 10-minute scan using a matrix size of 64 × 64 × 64 with isotropic three-dimensional resolution of 3.44 mm for a total field of view of (220 mm)^3 [13]. The sodium image at TE_1 was also used to quantify total sodium concentration (TSC) calibrated to the cerebrospinal fluid at 145 mM. The single-quantum sodium images were reconstructed off-line using custom-developed software. Since most (>60%) of bound sodium is from the intracellular compartment [14], we use the term intracellular sodium concentration (ISC) to refer to volume-fraction weighted concentration of bound sodium in this work for investigating therapy-induced changes of intracellular sodium concentration.

Image Analysis

PET images from both the BL and ETA scans of each subject were aligned and resliced to match the MPRAGE MRI scan from the subject's BL scanning session. A rigid registration was achieved using the normalized mutual information function available in the image analysis software PMOD 3.4 (University Hospital Zurich, Zurich, Switzerland). The result of this process is the coregistration of each subject's BL and ETA PET scans. F-18 ML-10 image activity was normalized by dividing by the mean activity within a large blood-pool region of interest (ROI) placed in the superior sagittal sinus.

Voxelwise Change Analysis

Identification of analysis voxels.   A loose tumor ROI that encompassed the entire tumor plus a margin of normal tissue but which excluded blood vessels, skull, and calvarium was manually placed around the tumor volume. For a voxel to be included in the voxelwise change analysis, it had to have significant uptake in at least one of the two scan time points (BL or ETA). Voxels within the ROI were classified as having significant F-18 ML-10 uptake if the activity within the voxel was greater than 5 SDs above the mean activity within a background ROI drawn in an uninvolved region of healthy tissue. The SD was calculated from all the voxels within the background ROI. The set of all voxels that were found to have significant activity at either BL or ETA time points is collectively referred to as the *voxel analysis domain*.

Fractional change in F-18 ML-10 uptake (*R*) was computed for each voxel in the voxel analysis domain as

$$R = \frac{C_{ETA} - C_{BL}}{\frac{1}{2}(C_{ETA} + C_{BL})}$$

where C_{ETA} and C_{BL} are the normalized ETA and BL F-18 ML-10 concentrations at the voxel. Because a voxel need contain significant activity at only a single time point to be included in the analysis do-

Table 2. Percentage of Change in Voxel Activity after Therapy.

Subject	% Voxels Increased	% Voxels Decreased	% Voxels With No Change
Subject 1	73.42	15.12	11.46
Subject 2	45.85	29.52	24.63
Subject 3	28.57	21.99	49.44

main, the average activity at BL and ETA is used in the denominator of *R* to avoid division by zero or small numbers.

Measures of change.   Voxels within the analysis domain were classified as increasing, decreasing, or unchanging between the ETA and BL scans on the basis of a 15% threshold. That is, voxels with $R > 1.15$ were deemed to have increased, and those with $R < 0.85$ were deemed to have decreased. The total numbers of increasing, decreasing, and unchanging voxels were separately tallied (Table 2). Spatial localization of increasing, decreasing, and unchanging apoptosis signals was accomplished by color-coded images. To identify possible additional features related to apoptosis changes from BL to ETA, a 2-dimensional (2D) histogram of ETA voxel value *versus* BL voxel value was produced for each subject. All voxels with significant uptake at either BL or ETA or both were included in the histogram.

Deformable Registration of Contrast MRI

MIM Software Inc (Cleveland, OH) has developed patent-pending technology that enables the operator to produce deformable registration and also allows the operator to guide deformable registration when there are large changes in anatomy by identifying the same anatomic landmark in both image volumes. Using this software, PET images from two time points can be co-deformed on the basis of CT or MRI deformation, which makes structures the same size and allows direct comparison of PET activity on a pixel-by-pixel basis. We employed this technology to a patient example (subject 4). Using the MIM 5.4 platform, a BL ROI was defined on the subject's BL F-18 ML-10 PET using the PET Edge tool, available in MIM 5.4, and transferred to the coregistered BL contrast-enhanced MRI. The BL T_1 contrast-enhanced MRI scan and associated F-18 ML-10 PET scans were co-deformed to the corresponding ETA T_1 contrast-enhanced MRI. The deformation transformation was applied to the ROI defined on the BL PET and overlaid on the ETA contrast-enhanced MRI.

Multimodal, Multitime-Point Assessment of Therapy Response

An ROI was defined on subject 4's ETA contrast MRI that included enhancing regions of the tumor. The MRI-defined tumor ROI was then applied to all F-18 ML-10 and total sodium imaging time points. Changes in F-18 ML-10 activity between BL and ETA time points were compared to changes in TSC. A voxelwise scatterplot comparing the change in these biomarkers was generated. Each point of the voxelwise change comparison scatterplot falls into one of four classes: I, corresponds to increased sodium concentration and increased F-18 ML-10 activity signal; II, corresponds to increased sodium concentration and decreased F-18 ML-10 activity; III, corresponds to decreased sodium concentration and decreased F-18 ML-10 activity; and IV, corresponds to decreased sodium concentration and increased F-18 ML-10 activity. Differences were spatially localized by assigning each voxel within the tumor ROI a particular color corresponding to scatterplot class.
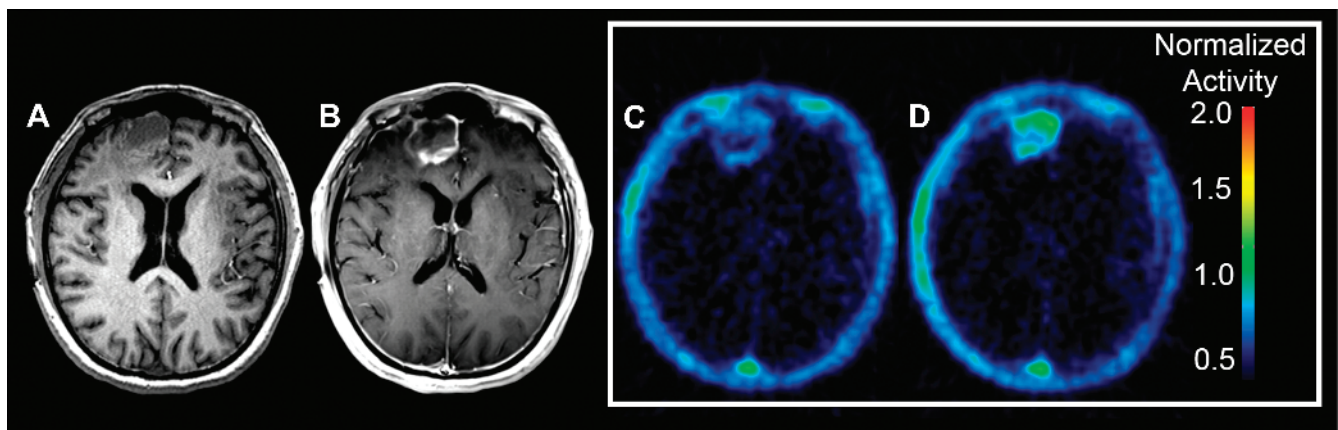
Figure 1. Representative BL MPRAGE MRI (A), contrast-enhanced MRI (B), BL F-18 ML-10 PET (C), and ETA F-18 ML-10 PET (D) images of subject 1 with right-frontal recurrent GBM. Both the BL and ETA (C and D) F-18 ML-10 PET scans show tracer accumulation that corresponds to the site of the GBM on the BL contrast MRI. Additionally, both the BL and ETA images show low nonspecific uptake in normal brain. The ETA scan shows increase in F-18 ML-10 uptake compared to BL.

Finally, spatial localization of the different biomarker change classes was accomplished by color-coded images.

Results

Figure 1 shows representative BL MPRAGE, BL contrast-enhanced MRI, and F-18 ML-10 images for a subject with a recurrent GBM (subject 1). Increased F-18 ML-10 uptake at ETA compared to BL is evident. In this case, tracer uptake on the PET image is observed to correspond to the site of the GBM on the BL contrast-enhanced MRI. We present this example as a case of a patient who ultimately had a good therapy response (Table 1). Both images show low non-specific uptake in normal brain.

Figure 2 shows representative BL and ETA contrast-enhanced MRI as well as BL and ETA F-18 ML-10 PET scans for two newly diagnosed patients with GBM. At BL, subject 2 (Figure 2C) shows a region of high F-18 ML-10 uptake in the center of the tumor located in the medial left temporal lobe with comparatively lower uptake observed on the tumor periphery. The ETA F-18 ML-10 PET scan (Figure 2D) shows a different pattern of tracer distribution compared
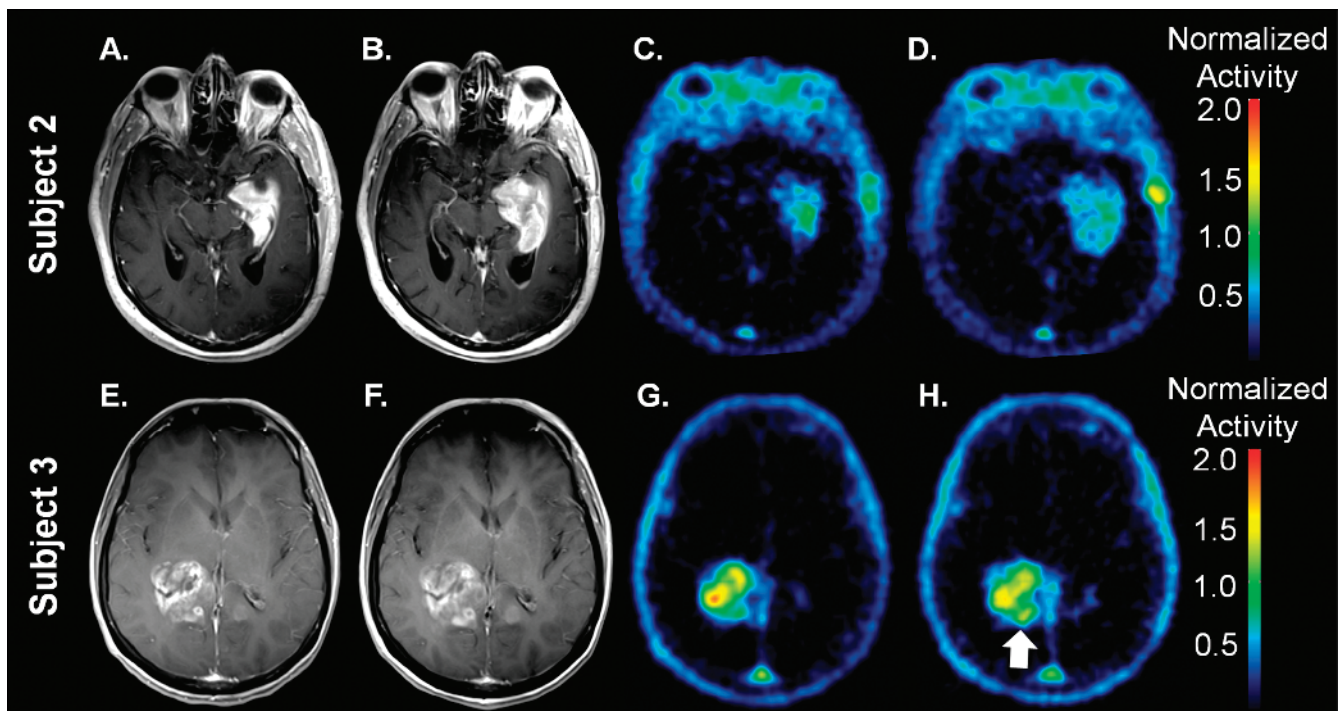

Figure 2. Representative BL (A and E) and ETA (B and F) contrast-enhanced MRI as well as BL (C and G) and ETA (D and H) F-18 ML-10 PET scans for subject 2 (A–D) and subject 3 (E–H). As described in the text, assessment of response based on qualitative visual interpretation or even by a semiquantitative index is ambiguous. Increased uptake on subject 3 ETA scan at the posterior medial border is indicated with an arrow.

to BL. Specifically, the initial region of high uptake at BL is observed to decrease, whereas regions of new F-18 ML-10 uptake are observed at ETA compared to BL. At BL, subject 3 (Figure 2*G*) shows focal, intense F-18 ML-10 uptake in the tumor region in the right posterior temporal lobe. The ETA F-18 ML-10 PET scan (Figure 2*H*) shows a different pattern of tracer distribution compared to BL. In this case, the uptake in the central portion has decreased, but a new region of F-18 ML-10 uptake is observed at the medial posterior border of the tumor (Figure 2*H*, *arrow*).

Taken together, these images are presented to illustrate challenges in evaluating therapy response in GBM using F-18 ML-10 PET on the basis of a qualitative visual interpretation. Whereas subject 1 (Figure 1) shows a desired global increase in F-18 ML-10 uptake after receiving therapy (Table 2), both subject 2 and subject 3 (Figure 2) exhibit a more complex, heterogeneous response. For example, although the initial region of highest F-18 ML-10 uptake is observed to decrease from BL to ETA for subject 2, a new region of tracer uptake is observed to appear at ETA on the tumor periphery. On careful inspection of the BL and ETA contrast-enhanced MRI, it is noted that compared to

BL, the size of the tumor at ETA is larger (Figure 2*B*) indicating new tumor and therefore tumor progression. On this basis, given the new tumor tissue, it is reasonable to suggest that the new uptake in this region is due primarily to tumor cell turnover associated with progression and not apoptosis associated with therapy response. This is further supported by the overall poor survival of subject 2 (Table 1).

Voxelwise Change Analysis

The observation that in one case voxels with BL F-18 ML-10 uptake increase in activity at ETA (Figure 1) indicating a good response, whereas in another case new regions of low F-18 ML-10 uptake at ETA spatially correlate with new regions of contrast enhancement (progression) on ETA MRI, compared to BL (Figure 2, *A* and *B*), suggests that a global analysis comparing numbers of voxels that increased or decreased (Table 2) may not be appropriate for response assessment. One strategy then is to quantify local, or voxelwise, changes in tracer uptake between BL and ETA time points. Figure 3*A* shows a scatterplot of ETA *versus* BL voxel activity for subject 2. Each color-coded circle represents a tumor voxel considered for analysis: voxels that decreased
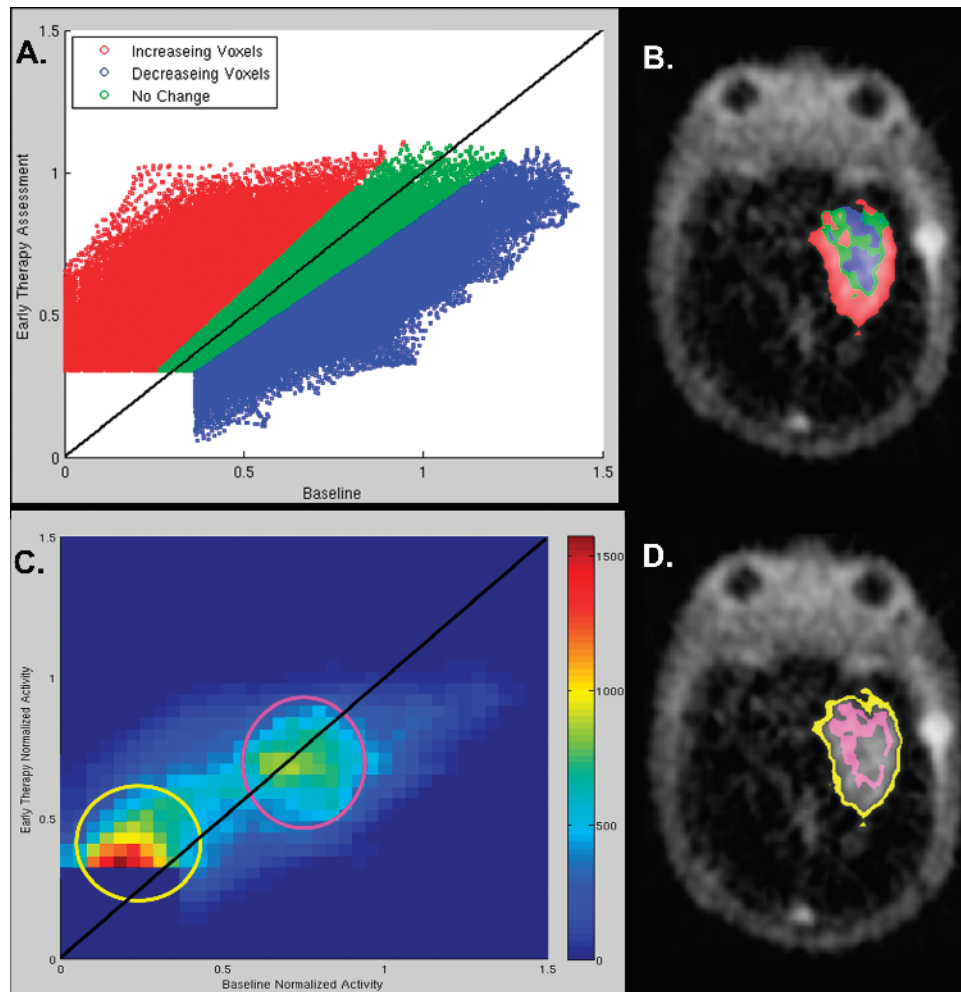

Figure 3. Voxel change maps for subject 2. A shows a voxel-by-voxel scatterplot of ETA *versus* BL activity, color coded to indicate voxels that decreased by more than 15% (blue), increased by greater than 15% (red), or neither increased nor decreased by 15% (i.e., unchanged; green). Plate (B) is a representative transaxial slice through the subject's tumor as seen on the ETA PET scan. The colors correspond to the change status of voxels between BL and ETA and have the same meaning as in A. The 2D histogram of plate (C) conveys similar information to that of the scatterplot (A). In plate (C), the density of points in the scatterplot is encoded by color. Plate (D) shows the spatial location (pink and yellow voxels) of two features (pink and yellow circles) seen in the 2D histogram of plate (C).
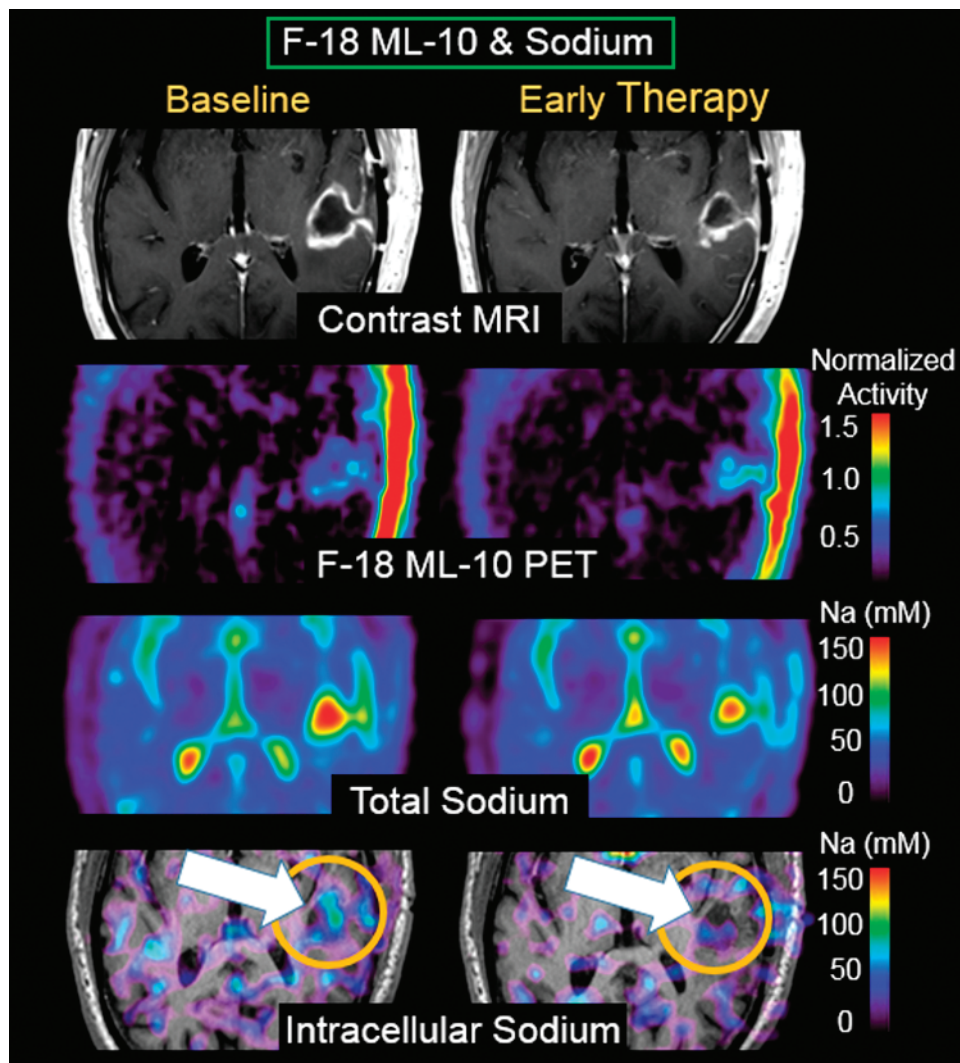
Figure 4. Same-day F-18 ML-10 PET and sodium MR scans at BL and ETA from subject 4. F-18 ML-10 (apoptosis) is observed to increase at the same location that intracellular sodium (proliferation) decreases (arrow). These results are interpreted as showing decreased proliferation at the same brain location as increased apoptosis.

by more than 15% (blue), increased by greater than 15% (red), or neither increased nor decreased by 15% (i.e., unchanged; green). Figure 3B shows a representative section of the voxel change map fused to the subjects' ETA F-18 ML-10 PET scan. The voxel change map spatially localizes voxels that increased, decreased, or did not change between BL and ETA imaging time points.

As a result of the small voxel size of the MPRAGE MRI, the individual points on the scatterplot (Figure 3A) are too numerous to visually distinguish point densities. Therefore, a 2D histogram (Figure 3C) was generated on the basis of the scatterplot to identify high-density regions of voxels. Comparison of the 2D histogram with the color-coded scatterplot shows which of the three classes those voxel densities belong. On the basis of visual inspection of the 2D histogram, two areas of high-density voxels were identified indicated by yellow and pink circles. To spatially identify where these voxels were located (Figure 3D), voxels within the two high-density regions were mapped to their locations on subject 2's ETA F-18 ML-10 PET scan. Voxels in the yellow region are observed to be located on the tumor periphery, whereas voxels in the pink region are observed to fall in the tumor interior.

Combined Imaging Biomarkers

In addition to identifying new regions of F-18 ML-10 uptake at ETA as either therapy-induced apoptosis or spontaneous apoptosis, additional challenges include distinguishing between a high percentage of apoptosis in a small density of tumor cells (e.g., F-18 ML-10 image is acquired after peak apoptotic response to therapy has occurred) *versus* a small percentage of apoptosis in a large density of tumor cells (e.g., native tumor apoptosis). This represents a challenge for molecular imaging using an apoptosis agent, because low tracer uptake due to effective therapy and low tracer uptake due to ineffective therapy may become indistinguishable. One approach to addressing this challenge is to integrate complementary functional biomarkers of cell viability from MRI as part of a subject's response assessment strategy. Figure 4 shows same-day F-18 ML-10 PET and sodium MR scans at BL and ETA for subject 4. Because the sodium MRI and F-18 ML-10 PET images are in alignment, each voxel at each imaging time point has associated F-18 ML-10 PET and sodium MRI values. F-18 ML-10 (apoptosis) is observed to increase at the same location that intracellular sodium (reflecting
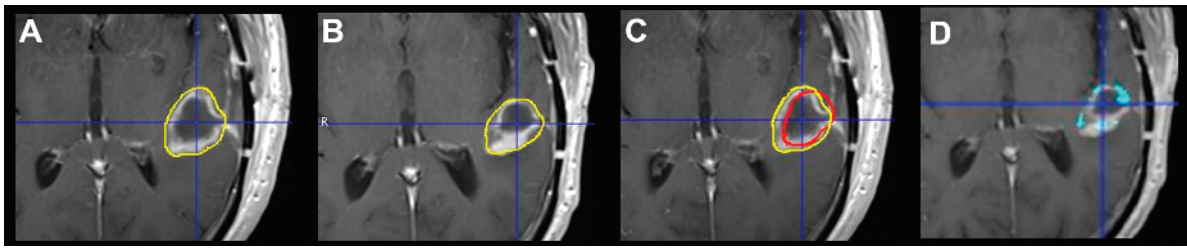
Figure 5. Contour deformation on subject 4. A BL ROI is defined on the BL F-18 ML-10 PET and transferred to the coregistered BL contrast-enhanced MRI (A). The BL contrast-enhanced MRI is then deformed to the ETA contrast-enhanced MRI, and deformation transformation is applied to the ROI defined on the BL PET. The deformed BL ROI is then overlaid on the ETA contrast-enhanced MRI (B). C shows the original undeformed ROI (yellow) and the deformed contour (red) overlaid on the undeformed BL contrast-enhanced MRI. D highlights regions of significant difference (blue) between the undeformed BL contour and the deformed ROI, overlaid on the ETA CE MRI.

activity of proliferation) decreases. These results are interpreted as showing decreased proliferation at the same brain location as increased apoptosis.

Deformable Registration for Accurate Subtraction Analysis

An approach to compensating for structural differences between images acquired at BL and ETA is to apply deformation matrices to PET data from contrast-enhanced T_1-weighted MR images, thereby ensuring that measures obtained at BL and ETA are from the same voxels. Figure 5 shows a demonstration of the deformable registration procedure. Deformable registration of contrast MRI scans was performed using the deformable registration tool available in the commercially available image analysis software MIM 5.4. A BL ROI was defined on the subject's BL F-18 ML-10 PET using the PET Edge tool and transferred to the coregistered BL contrast-enhanced MRI. Figure 5*A* show the coregistered ROI in yellow. The BL contrast-enhanced MRI was then deformed to the ETA contrast-enhanced MRI. The deformation transformation was applied to the ROI defined on the BL PET and is shown overlaid on the ETA contrast-enhanced MRI in Figure 5*B*. For comparative purposes, Figure 5*C* shows the original undeformed ROI (yellow) and the deformed contour (red) overlaid on the undeformed BL contrast-

enhanced MRI. Figure 5*D* further highlights differences in ROI definition methods. Specifically, regions of significant difference between the undeformed BL contour and the deformed ROI are highlighted in light blue and overlaid on the ETA contrast-enhanced MRI.

Multimodal, Multitime-Point Assessment of Therapy Response

Figure 6 demonstrates an example of a multimodal (F-18 ML-10 PET and sodium MRI), multitime-point (BL and ETA) assessment of GBM therapy response. Subject 4's ETA contrast MRI (Figure 6*A*) was used to define an ROI around the enhancing region of tumor. Changes in F-18 ML-10 activity between BL and ETA time points were compared to changes in TSC. Figure 6*B* shows a voxelwise scatterplot comparing the change in F-18 ML-10 and TSC biomarkers in the contrast-enhanced defined tumor ROI.

Discussion

Quantification of noninvasive *in vivo* imaging techniques to measure apoptosis is an important goal for the early detection of many disease processes in humans. To better understand the biologic underpinnings and imaging challenges central to the measurement of apoptosis, it needs to be recognized that the apoptotic process has unique properties
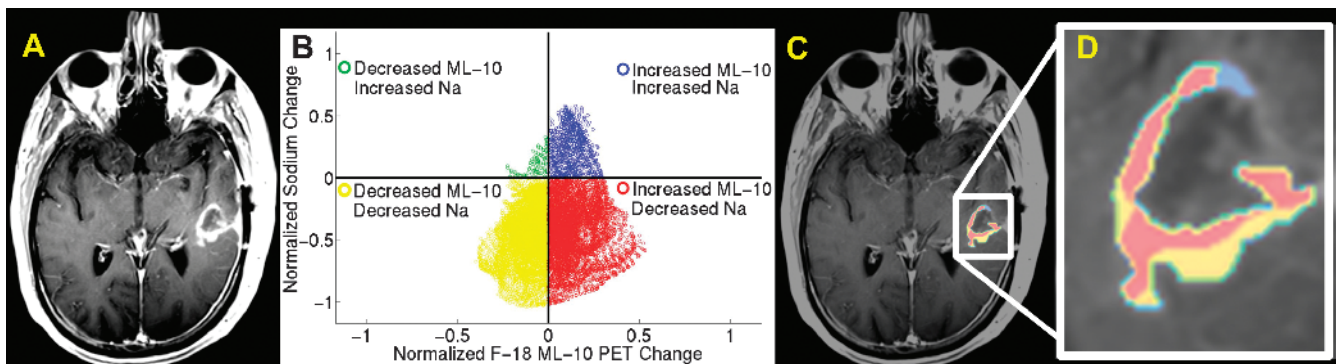

Figure 6. Example of a multimodal (F-18 ML-10 PET and sodium MRI), multitime-point (BL and ETA) assessment of GBM therapy response. Subject 4's ETA contrast-enhanced MRI (A) was used to define an ROI around the tumor. The ROI was applied to the same-time coregistered sodium (Na) MR and F-18 ML-10 PET scans at the BL and ETA time points. A scatterplot was used to evaluate multiparameter change for the contrast-enhanced MRI–guided ROI (B). Differences were represented in a four-quadrant scatterplot by assigning each voxel within the tumor ROI a particular color corresponding to scatterplot class (class I, blue; class II, green; class III, yellow; and class IV, red). To spatially localize changes, color-coded change maps were generated for the ROI volume and fused to the ETA contrast-enhanced MRI. Plate (C) shows a contrast-enhanced MRI section with the color-coded change parameters (color code is same as in B). Plate (D) shows a zoomed-in version of C.

that differ from other better understood "monotonic" molecular processes (such as reduction of F-18–labeled fluorodeoxyglucose uptake as a biomarker for reduced cellular metabolism) and imaging techniques currently employed for the assessment of therapy response in cancer [3,14]. Most importantly, apoptosis is an ephemeral process with a relatively short duration of existence between the time of initiation and ultimate cell death. Thus, the imaging challenge posed by this intrinsic dynamic change in tumor cell population apoptotic states must take this into account. Essentially, a population of cells undergoing apoptosis at BL will be nonexistent at follow-up, whereas a new population of cells will be undergoing new apoptosis as a result of effective therapy, but the net change in macroscopic signal may be little changed [9].

Therefore, it is evident that novel approaches to image quantification will be required to assess for therapy response, as typically measured by a change in tracer uptake distribution from BL to some time interval after therapy institution. In addition, timing following therapy is important, because time of apoptosis induction depends both on the specifics of the type of tumor cell, and therapy. Moreover, the heterogeneous tumor environment will likely play a key role in determining response to therapy, which introduces the requirement for a voxel-based analysis approach.

In addition to these challenges, neuro-oncology has additional difficulties. For example, intactness of the blood-brain barrier is a known issue with regard to transport of both PET tracers (e.g., F-18 fluorothymidine) and therapy. The analysis presented in this manuscript is a step on the road toward more refined methods that will incorporate early-time dynamic data, which may provide a method to identify regions with sufficient blood-brain barrier penetration. For example, one approach is to calculate the kinetic rate parameter K_1.

In this article, we have outlined imaging methods and analysis approaches that may afford investigators the opportunity to use this important imaging biomarker for the purposes of early therapy response assessment in cancer, specifically GBM. Procedures included commonly employed "standard" methods such as multimodality rigid image registration. However, the emphasis of this work is on less commonly used methods that could help to maximize the utility of apoptosis imaging. Although the complexity of apoptosis imaging accentuates the need for advanced image analysis techniques, traditional molecular imaging may also benefit from similar approaches.

A main tool used in the evaluation of overall therapy response between BL and ETA was tallying up changes occurring at an individual voxel level. Such procedures, compared to using average tumor quantities, may help to extract the spatially heterogeneous and temporally rapidly changing signal associated with the apoptosis process. An example of the use of values so determined is illustrated by Table 2, which lists whole-tumor indices deduced from a two–time-point, voxelwise analysis. Voxelwise analysis can also be used to provide parametric images and graphical representations of status changes, as illustrated by Figure 3. In this analysis, F-18 ML-10 activity change from BL to ETA for each voxel was normalized by the average of the BL and ETA activities on a voxel-by-voxel basis. This comparative approach was chosen to avoid division by small numbers as a result of very low F-18 ML-10 normal brain count activity. For example, if a voxelwise fractional change with respect to BL metric [e.g., (ETA – BL)/BL] is used to quantify change in activity between time points, subject 2 (Figure 2, *C* and *D*) would demonstrate a very high increase in activity at the periphery compared to BL, which could be falsely interpreted as apoptosis due to effective

therapy. In the case presented in Figure 2, the tumor increased in size (Figure 2, *A* and *B*), and the patient progressed (Table 1).

The use of a voxelwise analysis approach imposes some methodological impediments. In particular, image-registration accuracy is likely to be of consequence. Although intrasubject rigid registration methods are now relatively robust, the possibility of structural change in the interval between scans may impose a requirement for more sophisticated methods. A commercially available deformable registration method to address this was used for part of the data analysis. The results are illustrated in Figure 5. The application of deformable registration methods is intended to align the same tissue at two different time points. However, in light of the changing morphology associated with brain tumors, the utility of deformable registration for this purpose is limited. This method should be used with caution if there is a long time between BL and ETA scans or if there is an obvious significant anatomic change. In the future application of this approach, we anticipate that the time between the BL and ETA scans will be short, on the order of a few days. An advantage of apoptosis imaging is that we expect tumor apoptotic response to therapy, but not anatomic changes, to occur on this time scale [15].

A complication in apoptosis imaging for gauging therapy response is that image intensity is a function of both tumor density and apoptosis rate. For example, an increase in image intensity at any particular voxel could be due to increasing specific apoptosis rate (which, in a GBM early response assessment, would generally be considered favorable) or due to increasing tumor load (unfavorable) or to some combination. Resolving this confound requires additional information, for example, a measure of cellular proliferation. There are several possible approaches toward obtaining the required data. In this work, we made MR-based voxelwise measurements of changes in ISC. The joint results of sodium MR and F-18 ML-10 PET imaging are illustrated in Figure 4.

We note that the advent of dual-modality PET/MR may increase the clinical feasibility of obtaining joint imaging measures. Specifically, simultaneous 3T PET/MR is now possible in commercially available scanners. This can allow for same-time acquisition of other valuable biomarkers of therapy response, such as sodium. Although, to the date of drafting this paper, sodium imaging is not available on the integrated PET/MR scanners, it is likely to be available in the near future. The concentration of sodium is elevated in tumors relative to normal tissues due to increased intracellular sodium (reflecting membrane depolarization during mitosis and dysfunction of Na^+-K^+ pumps on the membrane) and/or an increased proportion of extracellular space (reflecting changes in cell morphology). Sodium MRI can exploit these properties to differentiate cancers from normal tissues with higher spatial resolution and signal to noise ratio than magnetic resonance spectroscopy [16] as well as assess changes in proliferative and/or cell volume fraction that occur in tumors and normal tissues after anticancer treatment. Triple-quantum filtering is usually used to detect the alteration of ISC, but it is limited in use due to its high specific absorption rate and long scan time (∼40 minutes at 3T) that is difficult for patients to tolerate. In the results shown here, we employed an alternative approach to intracellular sodium by using short-T_2 imaging method that produced low specific absorption rate and required a much (75%) shorter scan time than typical triple-quantum filtering imaging.

We propose a multimodal (F-18 ML-10 PET and sodium MRI), multitime-point (BL and ETA) approach to assessment of GBM therapy response. Figure 6 illustrates methods for displaying changes in complementary imaging biomarkers, in this case, sodium MRI

and ML-10 PET, from such an approach. In one display method (Figure 6B), differences are represented in a four-quadrant scatterplot by assigning each voxel within the tumor ROI (defined on the basis of a vascular parameter, in this case, contrast enhancement) a particular color corresponding to scatterplot class. In a second method (Figure 6C), spatially localized color-coded change maps are displayed on the ETA contrast-enhanced MRI. A future aim of our work is to correlate the two biomarkers with patient outcome. We speculate that patients exhibiting a relatively high F-18 ML-10 uptake and relatively low ISC (an example is of intracellular sodium; data is shown in Figure 4), both compared to BL, indicates a good response to therapy.

In conclusion, quantification of F-18 ML-10 brain scans may provide a novel approach for early response assessment and afford the patient's optimum management of their cancer therapy. Imaging apoptotic response to therapy is likely to require novel methods of analysis, and the purpose of this article was to lay foundation for that.

References

[1] Louis DN, Ohgaki H, Wiestler OD, Cavenee WK, Burger PC, Jouvet A, Scheithauer BW, and Kleihues P (2007). The 2007 WHO classification of tumours of the central nervous system. *Acta Neuropathol* **114**, 97–109.

[2] Dolecek TA, Propp JM, Stroup NE, and Kruchko C (2012). CBTRUS statistical report: primary brain and central nervous system tumors diagnosed in the United States in 2005–2009. *Neuro Oncol* **14**(suppl 5), v1–v49.

[3] De Saint-Hubert M, Prinsen K, Mortelmans L, Verbruggen A, and Mottaghy FM (2009). Molecular imaging of cell death. *Methods* **48**, 178–187.

[4] Aloya R, Shirvan A, Grimberg H, Reshef A, Levin G, Kidron D, Cohen A, and Ziv I (2006). Molecular imaging of cell death *in vivo* by a novel small molecule probe. *Apoptosis* **11**, 2089–2101.

[5] Reshef A, Shirvan A, Waterhouse RN, Grimberg H, Levin G, Cohen A, Ulysse LG, Friedman G, Antoni G, and Ziv I (2008). Molecular imaging of neuro-vascular cell death in experimental cerebral stroke by PET. *J Nucl Med* **49**, 1520–1528.

[6] Cohen A, Shirvan A, Levin G, Grimberg H, Reshef A, and Ziv I (2009). From the Gla domain to a novel small-molecule detector of apoptosis. *Cell Res* **19**, 625–637.

[7] Höglund J, Shirvan A, Antoni G, Gustavsson SÅ, Långström B, Ringheim A, Sörensen J, Ben-Ami M, and Ziv I (2011). ^{18}F-ML-10, a PET tracer for apoptosis: first human study. *J Nucl Med* **52**, 720–725.

[8] Oborski MJ, Laymon CM, Lieberman FS, Drappatz J, Hamilton RL, and Mountz JM (2014). First use of ^{18}F-labeled ML-10 PET to assess apoptosis change in a newly diagnosed glioblastoma multiforme patient before and early after therapy. *Brain Behav* **4**(2), 312–315.

[9] Allen AM, Ben-Ami M, Reshef A, Steinmetz A, Kundel Y, Inbar E, Djaldetti R, Davidson T, Fenig E, and Ziv I (2012). Assessment of response of brain metastases to radiotherapy by PET imaging of apoptosis with ^{18}F-ML-10. *Eur J Nucl Med Mol Imaging* **39**, 1400–1408.

[10] Blankenberg FG, Katsikis PD, Tait JF, Davis RE, Naumovski L, Ohtsuki K, Kopiwoda S, Abrams MJ, Darkes M, Robbins RC, et al. (1998). *In vivo* detection and imaging of phosphatidylserine expression during programmed cell death. *Proc Natl Acad Sci USA* **95**, 6349–6354.

[11] Sottoriva A, Spiteri I, Piccirillo SG, Touloumis A, Collins VP, Marioni JC, Curtis C, Watts C, and Tavaré S (2013). Intratumor heterogeneity in human glioblastoma reflects cancer evolutionary dynamics. *Proc Natl Acad Sci USA* **110**, 4009–4014.

[12] Marusyk A and Polyak K (2010). Tumor heterogeneity: causes and consequences. *Biochim Biophys Acta* **1805**, 105–117.

[13] Qian Y, Panigrahy A, Laymon CM, Lee VK, Drappatz J, Lieberman FS, Boada FE, and Mountz JM (2014). Intracellular sodium imaging in the brain via short-T2 component in bound sodium. *Proceedings of the 22th ISMRM Annual Meeting, Milan, Italy*. May 10–16, 2014. p. 2933.

[14] Winter PM and Bansal N (2001). Triple-quantum-filtered 23Na NMR spectroscopy of subcutaneously implanted 9L gliosarcoma in the rat in the presence of TmDOTP5-1. *J Magn Reson* **152**, 70–78.

[15] De Saint-Hubert M, Bauwens M, Verbruggen A, and Mottaghy FM (2012). Apoptosis imaging to monitor cancer therapy: the road to fast treatment evaluation? *Curr Pharm Biotechnol* **13**, 571–583.

[16] Ouwerkerk R (2007). Sodium magnetic resonance imaging: from research to clinical use. *J Am Coll Radiol* **4**, 739–741.